Design, Optimization, and Launch of a 3" Diameter N$_2$O/Aluminized Paraffin Rocket

Anthony McCormick, Eric Hultgren, Martin Lichtman, Jadon Smith, Ryan Sneed, and Shaun Azimi [1].
Stanford University, Stanford, CA, 94305

A 3-inch outer diameter hybrid sounding rocket was designed and built by Stanford University graduate students. The rocket was launched from the Mojave Desert. The rocket utilized a liquid N$_2$O oxidizer and a paraffin-based fuel that contained 40% aluminum powder by mass. Past experimental results show that adding aluminum to paraffin increases the combustion temperature and regression rate. Aluminizing the paraffin also decreases the optimal oxidizer to fuel ratio, making it possible to reduce the volume of the oxidizer tank relative to straight paraffin hybrid rockets. A constrained nonlinear least squares algorithm was used in conjunction with a one degree of freedom trajectory simulation to optimize mechanical design parameters for highest apogee altitude. Altitude performance was also improved by development of an innovative external valve actuation system that reduced the overall weight of the rocket by eliminating the need to carry an actuator onboard. A novel launch stand using spring mounted wheels to guide the rocket eliminated the need for launch lugs, thereby reducing drag. This paper provides detail of the rocket design, including an itemized mass budget, trade studies and sensitivity analyses, launch infrastructure, cost, and flight data for a flight reaching 9,400 feet above ground level.

Nomenclature

A_e	=	nozzle exit area	I_{sp}	=	specific impulse
A_{inj}	=	injector cross-sectional area	I_t	=	total impulse
A_t	=	nozzle throat area	L	=	combustion port length
a	=	regression rate coefficient	M	=	Mach number
β	=	drag multiplier	m	=	total mass of rocket
C_d	=	discharge coefficient	$\dot{m}$	=	mass flow rate
C_D	=	coefficient of drag	n	=	flux exponent
C_F	=	thrust coefficient	O/F	=	oxidizer to fuel ratio by mass
c^*	=	characteristic velocity	ρ	=	density
D	=	drag	P	=	pressure
D_f	=	final port diameter	q	=	dynamic pressure
D_i	=	initial port diameter	R	=	combustion port radius
DOF	=	degree of freedom	$\dot{r}$	=	regression rate
D_p	=	port diameter	S_{ref}	=	aerodynamic reference area
γ	=	ratio of specific heats	T	=	thrust
g_o	=	acceleration due to gravity at sea level	T_{vac}	=	vacuum thrust
G_{ox}	=	oxidizer mass flux	t	=	time
η_{Isp}	=	impulse efficiency factor	w	=	weight
h	=	altitude	V	=	volume

I. Introduction

A hybrid rocket propulsion system uses a liquid oxidizer and a solid fuel propellant to incorporate the high thrust-to-weight ratio of solid rockets and the high specific impulse of liquid rockets. Hybrid propulsion systems also offer increased safety because the fuel and oxidizer are in different phases, and will be less likely to

---

[1] Graduate Students, Department of Aeronautics and Astronautics, Stanford, CA 94305, AIAA Student Members.

mix in the event of a leak. Historically, however, hybrid rockets have had limited applications because of slow fuel regression rates. Recently, Dr. M. Arif Karabeyoglu at Stanford University identified paraffin wax a new high regression rate fuel that may open up many new applications.

Paraffin-based hydrocarbon fuels have shown regression rates three to four times higher than conventional polymeric hybrid fuels. These results have been confirmed in both lab-scale and scaled-up tests at Stanford University and NASA Ames Research Center. The paraffin fuels have demonstrated comparable specific impulse performance and favorable density impulse performance to hydrocarbon fueled liquid systems.[1]

Aluminization of the paraffin fuel grain has been experimentally shown to further increase the regression rate. The regression rate law for hybrid systems can be expressed as[2]

$$\dot{r} = aG_{ox}^n \tag{1}$$

Previous experimental data give values of $a = 0.155$ mm/s and $n = 0.5$ for paraffin/nitrous oxide systems.[1]

Initial research on 40% by mass aluminized paraffin fuel indicated an a value 10% greater than that of pure paraffin. Additional data from aluminized paraffin experiments at Stanford estimated the increase in regression rate at 25%. Further testing is still needed to gain sufficient confidence in this parameter.

Research for this publication was conducted in the context of a hybrid rocket design program at the Department of Aeronautics and Astronautics at Stanford University. The authors were charged with the mission requirements of demonstrating an innovative propulsion system with a target altitude of 10,000 ft. using an airframe of no more than 3" diameter. This paper gives significant weight to the design process and the design details, with the goal of providing useful information for other small rocket programs, in addition to performance data for the aluminized paraffin propulsion system.

II. Preliminary Design

The design of the propulsion system for the rocket was influenced by several considerations. Program requirements included that the airframe could be no wider than 3" diameter, and that the fuel and oxidizer would be non-cryogenic, non-carcinogenic materials. For performance considerations, it was desirable to have a high impulse-to-weight ratio. For structural and aerodynamic considerations, it was desirable to minimize the size of the propulsion system.

A. Fuel Selection and Volumetric Efficiency

A trade study was performed to determine the desired aluminum content of the fuel. Consider the following equation for specific impulse I_{sp}

$$I_{sp} = c^* C_F / g_0 \tag{2}$$

In this equation, c^* is the "characteristic velocity," a function of the propellant and combustion chamber design.[2] For operation near sea level, the total impulse of the system is given by

$$I_t = I_{sp} w \tag{3}$$

where w is the weight of the expended propellant. Assuming a fixed total impulse for the propulsion system and identical (and constant in altitude) C_F for both systems, the ratio of weight of the 40% aluminum paraffin fuel to the pure paraffin can be written as

$$\frac{w_{40\% Al}}{w_{0\% Al}} = \frac{c^*_{0\% Al}}{c^*_{40\% Al}} \tag{4}$$

The Air Force Chemical Equilibrium code[3] was used to calculate c^* for paraffin with various aluminum concentrations as a function of O/F ratio at a fixed pressure (See Fig. 1).
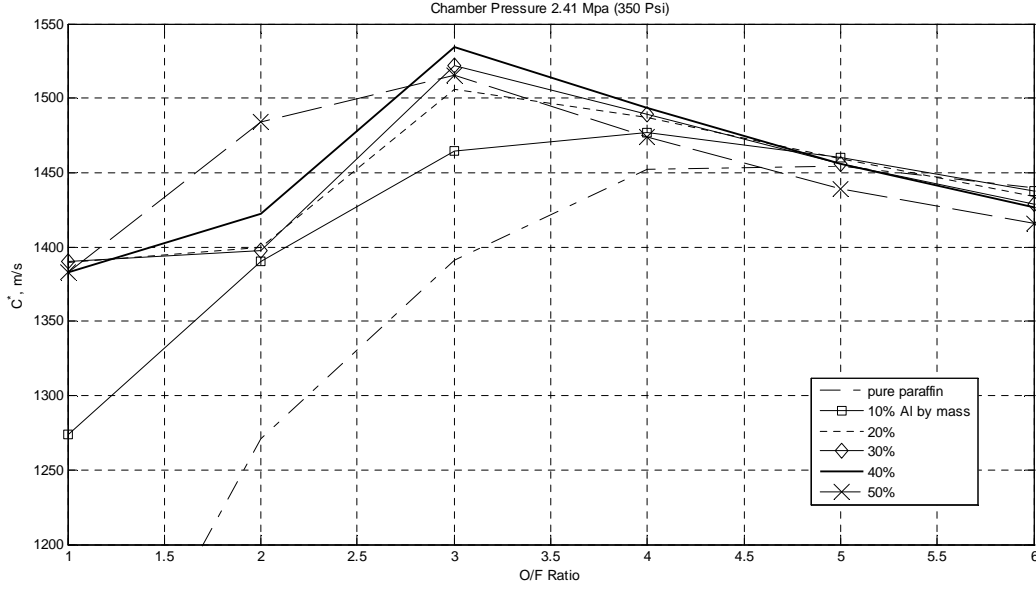
Figure 1. c^* of aluminized paraffin vs. O/F ratio from the CEA code.

The data imply that the global maximum characteristic velocity is obtained with 40% aluminum content and an O/F ratio of about three. At that point, c^* is 1,534 m/s. By contrast, pure paraffin has a maximum of 1,454 m/s at an O/F ratio of 5. Therefore, for a given total impulse, the 40% aluminum paraffin motor weighs about 5% less than the pure paraffin motor.

The volume reduction achieved with aluminized paraffin is of equal importance. The densities of saturated liquid N_2O, paraffin, and 40% aluminized paraffin are taken to be 1,222 kg/m^3, 930 kg/m^3 and 1,250 kg/m^3, respectively. The relationship between the volumes of the two systems is expressed as

$$\frac{V_{40\%}}{V_{0\%\,Al}} = \frac{w_{40\%\,Al}}{w_{0\%\,Al}} \left[\frac{\dfrac{1}{\rho_{40\%\,Al}} + \dfrac{\left(O\!/\!F\right)_{40\%\,Al}}{\rho_{N_2O(l)}}}{\dfrac{1}{\rho_{0\%\,Al}} + \dfrac{\left(O\!/\!F\right)_{0\%\,Al}}{\rho_{N_2O(l)}}} \right] \tag{5}$$

If both systems operate constantly at optimal O/F ratio, then the system using aluminized paraffin is only 60% as voluminous as the pure paraffin system. Given a fixed inner diameter for the pressure vessels, and only considering the oxidizer tank and the combustion chamber, the aluminized system will therefore only be 60% as long as a pure paraffin system. The effect of varying combustion chamber length on combustion efficiency has not yet been adequately studied; for the sake of the preceding calculations, the effect was not included.

B. Aerodynamics and Trajectory Simulation

The preceding analysis relied on several simplifying assumptions, chiefly that O/F ratio, c^* and C_F are constant throughout the flight. In reality, O/F ratio is a function of port diameter and oxidizer mass flow rate. O/F ratio increases in time while oxidizer mass flow rate decreases in time. The characteristic velocity is a function of combustion chamber pressure and combustion efficiency, neither of which is constant. Lastly, C_F is a function of ambient pressure thus it changes with altitude.

A simple 1-DOF simulation was developed in MATLAB to aid the design process with the aim of maximizing apogee altitude, the main performance metric. The equation of motion was derived from a flat-earth model for gravity, a standard model for atmospheric properties (density, temperature, and pressure), a drag model and a motor model.

The drag model was obtained using Missile DATCOM[4], with results confirmed using another software package, Aerolab[5]. Figure 2 shows the coefficient of drag with reference to the main-body cross sectional area. High skin friction at low Mach numbers causes the first peak, and the transonic drag rise is seen in the second peak. The coefficient of drag for the unpowered rocket is higher because without the combustion exhaust, a region of low-pressure recirculating flow exists aft of the rocket base.
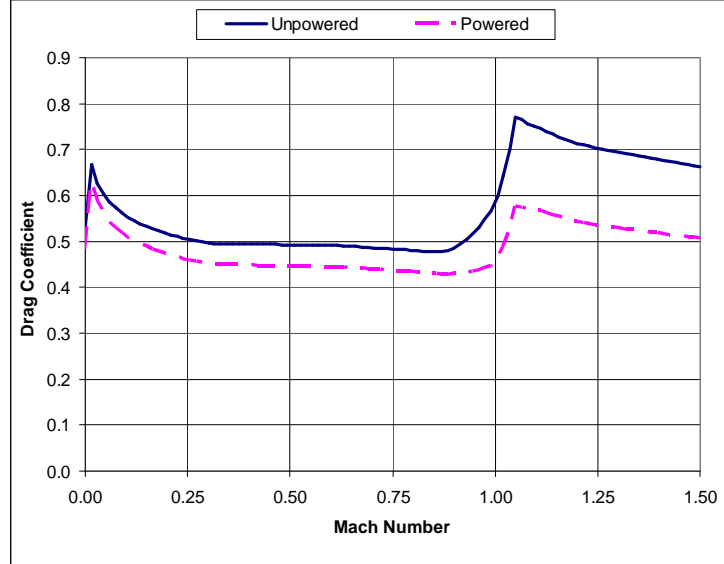

Figure 2. Aerolab drag predictions.

Assuming a constant pressure difference across the injector, the oxidizer mass flow rate was calculated from the pressure difference between the oxidizer tank and the combustion chamber using an experimentally-determined discharge coefficient C_d:

$$\dot{m}_{ox} = C_d A_{inj} \sqrt{2 \rho_{N_2O}(P_{ox} - P_c)} \qquad (6)$$

Here, P_{ox} and P_c are the oxidizer tank pressure and combustion chamber pressure, respectively. The motor model assumed P_{ox} and P_c to be constant in time, although testing revealed this to be a poor approximation (see Fig. 11 for plots of pressure versus time for both pressure vessels). The fuel mass flow rate was computed using Eq. (7).

$$\dot{m}_{fuel} = \rho_{fuel} D_P L \left(a G_{ox}{}^n \right) \qquad (7)$$

With the mass flow rates of oxidizer and fuel known, the O/F ratio is used to calculate c^* from the curve in Fig. 1. In order to calculate the "vacuum thrust" T_{vac}, isentropic "frozen" flow in the nozzle is assumed, and Eq. (8) is used to determine the pressure at the nozzle exit P_e. The exit Mach number M_e is determined from the nozzle geometry alone, assuming the flow through the nozzle is choked. Equation (9), where P_a is the ambient pressure, A_e is the area of the nozzle exit, and A_t is the area of the nozzle throat, is then used to find T_{vac}.

$$P_e = P_c \left[1 + \frac{\gamma - 1}{2} M_e{}^2 \right]^{\frac{-\gamma}{\gamma - 1}} \qquad (8)$$

$$T_{vac} = \left[\frac{2\gamma^2}{\gamma-1} \left(1 - \left(\frac{P_e}{P_c}\right)^{\frac{\gamma-1}{\gamma}} \right) \left(\frac{2}{\gamma+1}\right)^{\frac{\gamma+1}{\gamma-1}} \right]^{\frac{1}{2}} + \frac{P_e A_e}{P_a A_t} \tag{9}$$

Thrust can be calculated from the vacuum thrust by Eq. (10). An impulse efficiency factor η_{Isp} of 0.77 was used to represent a compounded loss of thrust due to nozzle friction and geometry, incomplete combustion, and other effects.

$$T = \eta_{Isp} T_{vac} - P_e A_e \tag{10}$$

C. Sensitivity and Optimization

A large number of simplifying assumptions were made for the MATLAB optimization, but only a few are mentioned here. The key assumptions and constraints were:

- The mass of the rocket including fuel and payload was 15 kg (obtained by scaling down the mass for the hybrid rocket of Van Pelt, et al.[6]).
- The rocket length was a no more than 40 times the main body diameter (for flexural stability).
- The oxidizer mass flow rate into the combustion chamber was constant during powered flight.
- Powered flight terminated when the inner diameter of the fuel grain reached the outer diameter (minus a predetermined sliver fraction for safety margin).
- Final port diameter of the fuel grain D_f was constrained by the combustion chamber geometry.
- The flight path was vertical.

Using the simulation, the altitude of apogee was calculated using a 4th-order Runge-Kutta method to integrate the equation of motion. The resulting apogee altitude h is a nonlinear function of multiple variables.

$$h = f(L, D_i, D_f, ...) \tag{11}$$

A Gauss-Newton Nonlinear Least Squares (NLSQ) algorithm, with inequality constraints, was used find the geometric parameters that maximize the apogee altitude h. It has not been proven that f is a convex function with one global maximum; however, given an initial guess for the design parameters, the algorithm can be used to improve the result.

While some design parameters were constrained by availability of materials and other considerations, others, in particular D_i and nozzle area ratio, were selected using the algorithm to optimize apogee altitude. Consider nozzle area ratio A_e/A_t. The optimal expansion ratio can be determined analytically for the assumption of choked flow, fixed combustion chamber pressure, quasi-one dimensional isentropic flow, and fixed ambient pressure.[2] However, because ambient pressure varies with altitude, the optimal area ratio for the entire flight is difficult to determine analytically. The NLSQ algorithm provided a numerical calculation of the best area ratio.

Figure 3 illustrates how the gradient-based algorithm found a local optimum that maximized the altitude based on a combination of parameters. It can be seen from the figure that, in the trade space of initial port diameter and nozzle area ratio, with other parameters taken to be constant, the design configuration gives very nearly the best possible performance. It should be noted, however, that the simulation substantially over-predicted the apogee altitude. Also, the simulation was revised several times over the course of the project, accounting for the disparity between the optimal inner port diameter and the port diameter as it was made. Future design iterations should use a refined model for the optimization algorithm.
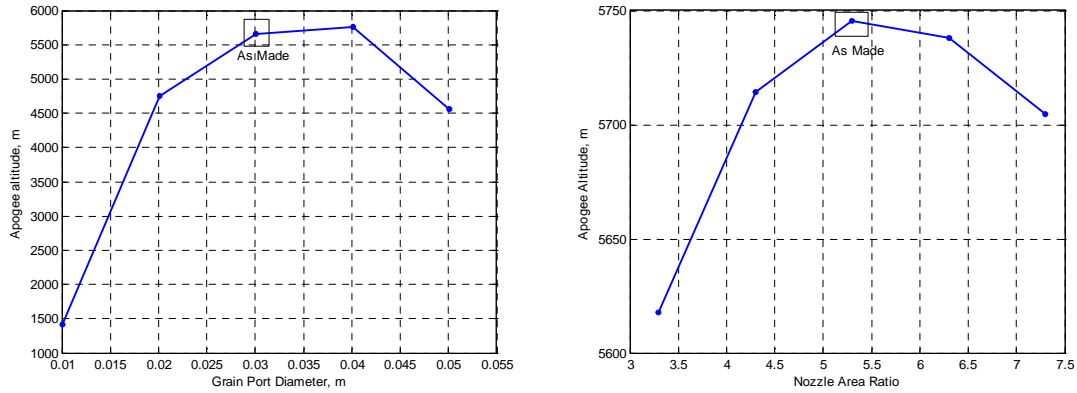
Figure 3. Optimization of grain port diameter and nozzle area ratio.

Additional simulation of the sensitivity of apogee altitude to weight and drag was performed. The results are plotted in Fig. 4:
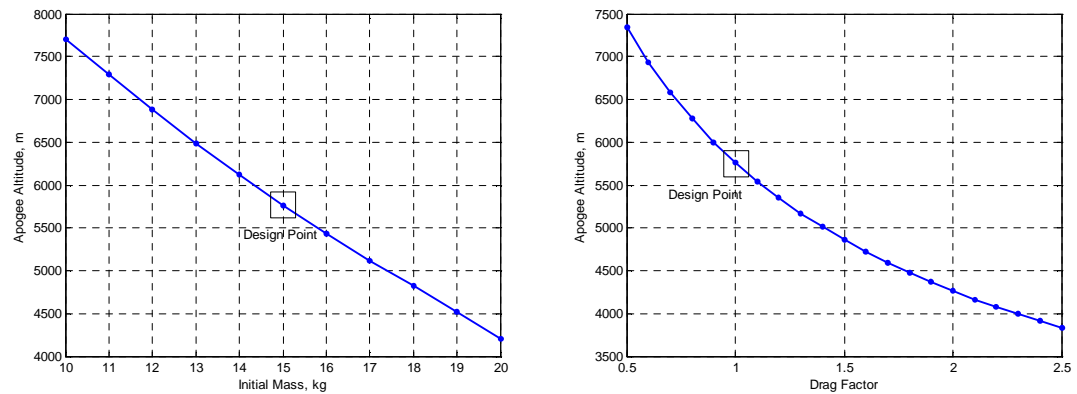

Figure 4. Estimated sensitivity of apogee altitude to mass (left) and drag (right).

III. Detailed Design

A. Launch Equipment

The sensitivities given in the previous section show that over the flight regime the apogee altitude was very sensitive to weight and drag. Thus, minimizing these two properties was a major focus of the project. To reduce drag, the rocket was designed to minimize the number of flow disturbances. The most pronounced disturbance comes from launch lugs, which are part of a conventional sounding rocket launch system. The drag coefficient increases by approximately 5% if lugs are included in the aerodynamic model.

1. Lugless Launch Stand

To eliminate the drag caused by launch lugs, Van Pelt, et al.[6] employed a launch stand that used three guide rails that butted up against the rocket for directional guidance during launch. Two improvements were made on this design. First, low-friction guide wheels with internal 868 ball bearings replaced the three guide rails. Second, wheels were spring mounted to allow for passage of a rocket of potentially varying diameter. The polyurethane inline skate wheels provided directional guidance without adding unnecessary friction in the vertical direction. The spring mounts were critical because the rocket was designed with an aft flange. This system allowed for minimal friction in the vertical direction (less than a launch lug system), lower rocket weight, lower rocket drag, and significant traction against rotation during launch. Wheels were mounted two-per-axle, with three axles 120° apart. There were three sets of three axles along the length of the rocket located approximately 3 ft. apart: at the middle of the combustion chamber, top of the oxidizer tank, and just aft of the nose cone.

*2. Externally Actuated Oxidizer Flow Valve*

To reduce weight and minimize flow obstructions, the oxidizer flow was controlled with a single ball valve between the oxidizer tank and the combustion chamber. A commercial-off-the-shelf 3/8" full-port ball valve was

chosen for its well-defined flow characteristics and certified pressure rating. The ball valve was actuated by a heavy pneumatic motor, which was in turn powered by 100 psi air from a compressor. However, the weight and size of this system were not an issue because these parts were integrated into the launch stand, not the rocket. This was accomplished by a mechanism that disengaged and retracted from the rocket after actuation.

The actuator was designed to engage the ball valve handle during the 90° clockwise rotation from the "closed" position to the "open" position. This actuation occurred within 0.15 seconds, and was followed by an immediate 90° counterclockwise rotation. The ball-valve-to-actuator interface was designed so that the actuator did not engage the ball valve handle during this counterclockwise rotation. This relieves the torque that would otherwise have caused binding, allowing the actuator to retract. In its retracted position, the actuator does not obstruct the rocket's motion. The pneumatic motor is mounted on a hinge, and after disengaging from the ball valve handle, the mechanism pivots away from the rocket under its own weight. The pivoting motion is in the upward direction near the rocket, so no interference with the rocket could occur during launch.

The only drawback to the external actuation technique was that the interface to the ball valve must be externally accessible, creating a drag-inducing protuberance. A modification of the ball-valve-to-actuator interface allowed the valve to be opened and closed during the oxidizer filling process.

A schematic of the launch equipment operation is shown in Fig. 5; a photograph of the ball valve as mounted on the oxidizer tank is shown in Fig. 6.
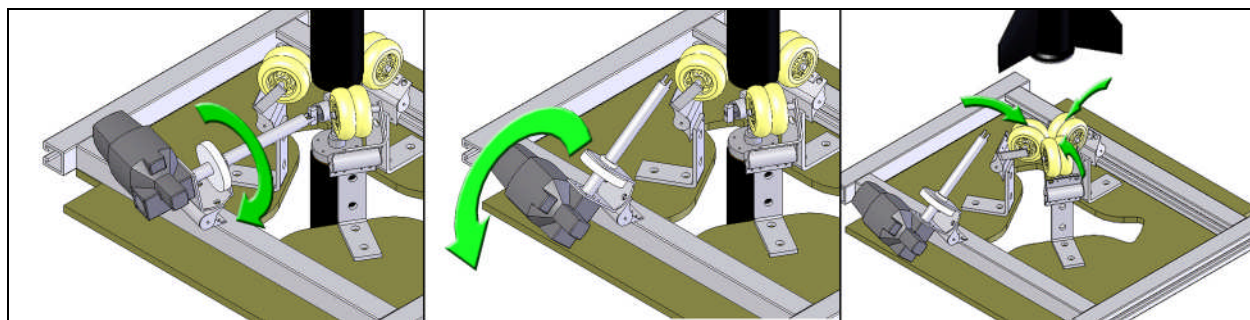
a) Actuator turns valve to open ,   b) Actuator and arm fall away,   c) Wheels conform to rocket body
Figure 5. External actuation system and guidance wheel operation (shown without midsection fairing for clarity).
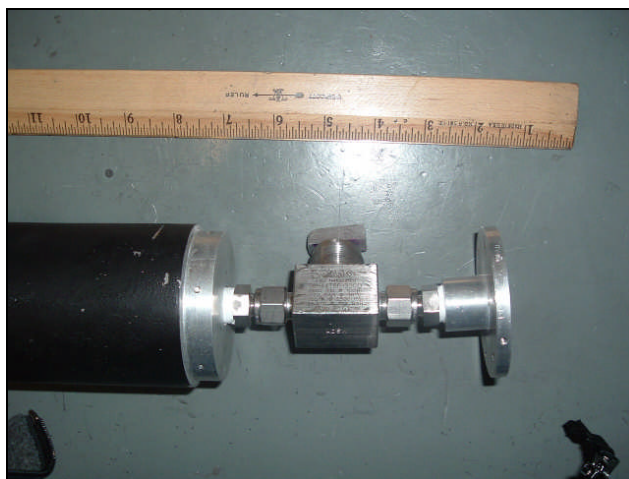

Figure 6. The 3/8" full-port ball-valve mounted on the oxidizer tank.

B. Motor

The motor aft of the ball valve consisted of an aluminum injector body, a copper injector plate, the aluminum combustion chamber, a high-density polyethylene (HDPE) pre-combustion chamber, the aluminized paraffin grain which was cast in a thin polycarbonate liner, a conical graphite nozzle, and an aluminum retention ring. A schematic of this portion of the propulsion system is shown in Fig. 7. The initial port diameter D_i was 35.2 mm, the final port

diameter D_f was 67.85 mm, the grain length was 300.2 mm, and the nozzle expansion ratio A_e/A_t was approximately 5.3.

Since the mission called for multiple flights in a short amount of time, the motor design was intended to be highly modular to increase the ease of disassembly in the field. At the fore end of the chamber, the injector body and head were mounted using six machine screws. Removal of the injection system allowed for pre-flight inspection of the igniters. At the aft end of the chamber, a retention ring was mounted onto a flange by nine machine screws.
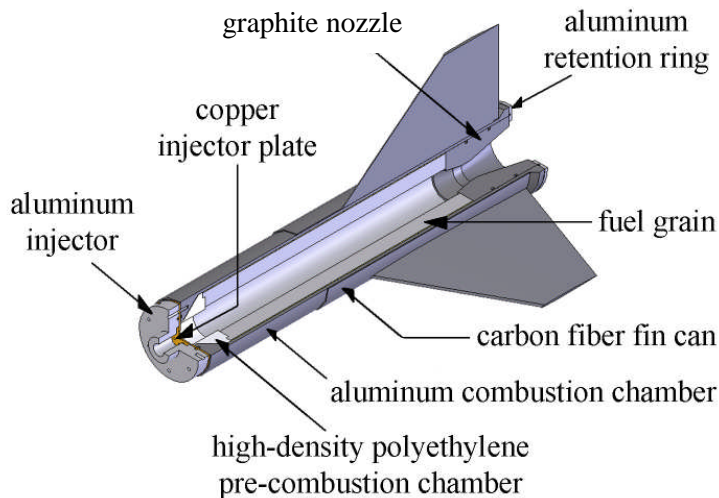

Figure 7. Motor schematic.

A showerhead-style 1/16" thick copper injector plate was selected for three major reasons. First, the geometry allowed for a minimal addition of weight. Second, copper is an oxidizer-safe material. Third, the design could be easily tuned to optimize oxidizer flow rate and discharge coefficient. Based on oxidizer flow testing, the final design consisted of a 13-hole pattern with a central hole, 6 holes on a ½" diameter circle, and the remaining 6 holes offset from the inner ring on a 1" diameter circle. Each individual hole diameter of 0.067" was a compromise between better oxidizer atomization and the avoidance of cavitation.
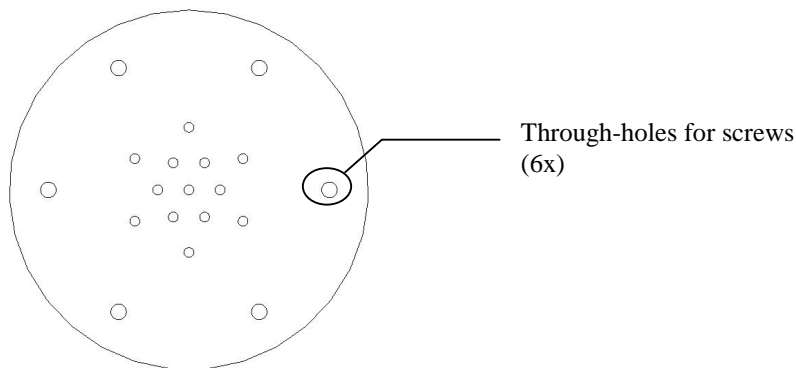

Figure 8. 13-hole injector plate (outer holes used for mounting).

C. Ignition System

The ignition system laid out in Fig. 9 has two basic functions: to light the igniters and start the flow of oxidizer with a precise time delay between the two events. The initiation and sequencing of these events were controlled electronically with a fire control box. The box was commanded remotely via a full-duplex wireless data link. The software allowed for opening and closing the oxidizer valve for filling with the actuator mechanism, opening and closing the vent solenoid valve to bleed oxidizer over-fill, and executing the launch sequence.
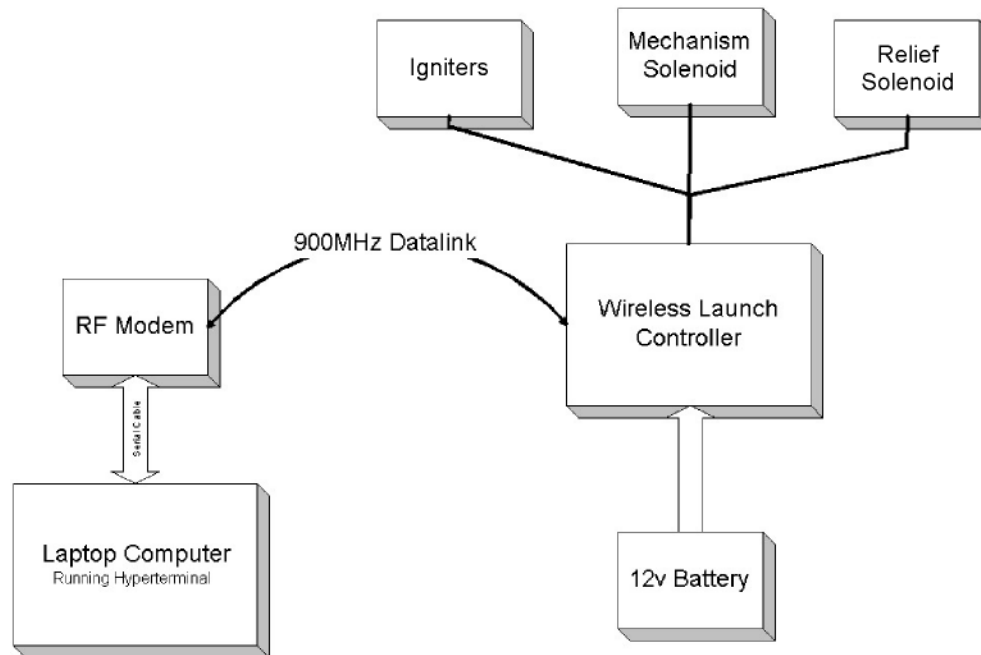
Figure 9. Electronic hardware block diagram.

A wireless data link was used for several reasons: safety, flexibility, and reliability. The wireless system incorporated the following features:

- Frequency-hopping spread spectrum (FHSS)
- 32-Bit error checking
- Data acknowledgement protocol
- 38,400 bits per second data rate
- 1,000 ft. line of sight communication range

A small amount of ammonium perchlorate-based solid fuel, cut from a model rocket engine, was used to start the hybrid motor. These engines are sold by Aerotech, Inc. under the label "Blue Thunder." Two 29 mm diameter discs of solid fuel were epoxied to the inside of the pre-combustion chamber. The solid fuel was ignited using Estes electric matches, embedded in the solid fuel. The electric matches require a high current at 12 V in order to reliably fire.

The launch sequence begins with the firing of the electric matches, followed by a programmable delay, before initiation of oxidizer flow. The igniters must be lit first in order to pre-melt the fuel grain and start vaporizing the paraffin. The timing of the entire launch sequence is shown in Table 1.

Table 1.   Launch Sequence.

Event	Time Delay, s
Ignition of electric matches	0.0
Clockwise actuation of oxidizer valve	0.3
Counter-clockwise disengagement of actuator	0.5

D. Recovery System

Recovery was effected by a two-stage parachute deployment mechanism. The first stage, designed to be deployed at apogee, consisted of a circular 48" drogue parachute. The second stage, designed to be deployed at 1,500 feet above ground level, consisted of a larger parachute to slow the rocket's descent rate to roughly 5 m/s. Both parachutes were obtained commercially.

Deployment was handled by a commercially available device called the G-Wiz MC. The G-Wiz has a single axis accelerometer and absolute pressure sensor, as well as EEPROM to store 5 minutes of telemetry data at 4 Hz and three high current switches. It is powered by two 9 V prismatic alkaline cells, which provide power for the G-Wiz

and the high current pyrotechnic channels. The first channel was powered at apogee, activating a CO_2 canister that pressurized the airframe and caused separation of the nose cone from the fore body, releasing the drogue parachute. The second channel was connected to a tether-cutting mechanism to release the main parachute. After cutting the tether, the main parachute was to be drawn out of the airframe by the drogue. The tether-cutting mechanism consisted only of a length of chromel wire entwined with fishing line, which was in turn wrapped around a metal hasp that tightly clamped the main parachute packing bag. On activation of the low-altitude channel, the wire melted the fishing line, which released the hasp to release the main parachute. Although bench tests of the recovery system were successful, the main parachute failed to open during flight due to a packing error. However, the drogue parachute showed it could provide nearly adequate deceleration, and the rocket was intact, with only minor damage.

The nose cone of the rocket was secured to the airframe by a friction fit, with a liberal amount of museum wax to increase the coefficient of friction and improve the pressure seal on the parachute compartment.

E. Airframe and Camera

The airframe consisted of two aluminum pressure vessels (1/8" wall thickness) in line with the paper phenolic payload section and polyethylene nose cone. Integrated into the nose cone were flight avionics and an aft-looking Aiptek DV2 digital video camera. The camera was chosen because it records to solid state flash memory, making it survivable under the rigors of a rocket launch. The onboard video can be viewed on the web site listed at the end of this paper. The plane of separation for the recovery system was located just aft of the camera.

A carbon fiber 3-fin can was used. The fins were sized to ensure a 10% static stability margin for all flight Mach numbers and for all possible distributions of fuel and oxidizer. For reference, a comprehensive list of the components and their masses is given in Table 2 in the Appendix.
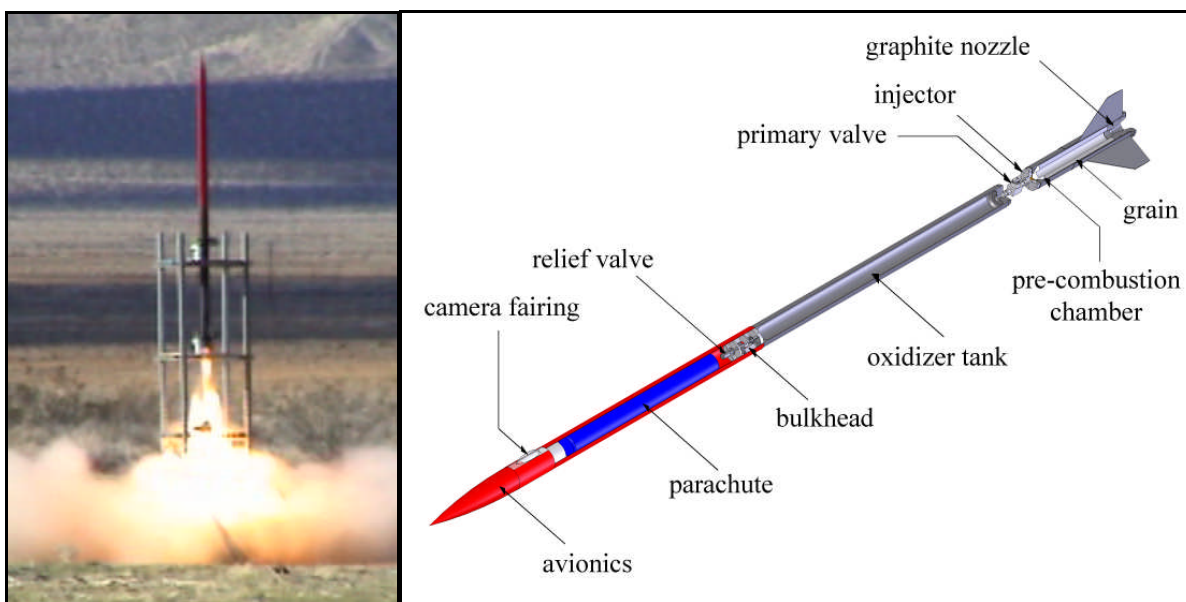

Figure 10. Final rocket design.

IV. Ground Test Program

Once the final design was completed, understanding the true motor performance rather than the designed to performance was critical. This was accomplished through a detailed ground testing program that included four cold flow and three static motor tests.

A. Cold Flow Testing

The cold flow tests were performed to measure and improve oxidizer mass flow rate $\dot{m}_{ox}$ and discharge coefficient C_d through the injector, as well as to verify oxidizer loading procedures and valve operation.

$$C_d = \frac{\Delta m}{\Delta t A_{inj} \sqrt{2 \rho_{ox} \Delta P}}$$ (12)

Once C_d was determined, $\dot{m}_{ox}$ could be calculated from Eq. (6).

To achieve a significant back pressure build-up in the combustion chamber without ignition, a reduced nozzle port area was used. Initial testing indicated a very low mass flow rate of 0.19 kg/s and an unacceptable discharge coefficient of 0.14. This low C_d value was attributed to cavitation of the nitrous oxide at the injector plate. After increasing the shower head orifice diameters and total injector area, an acceptable discharge coefficient of 0.42 and mass flow rate of 0.68 kg/s were obtained. Pressure histories for two of the blowdown tests are shown in Fig. 11.
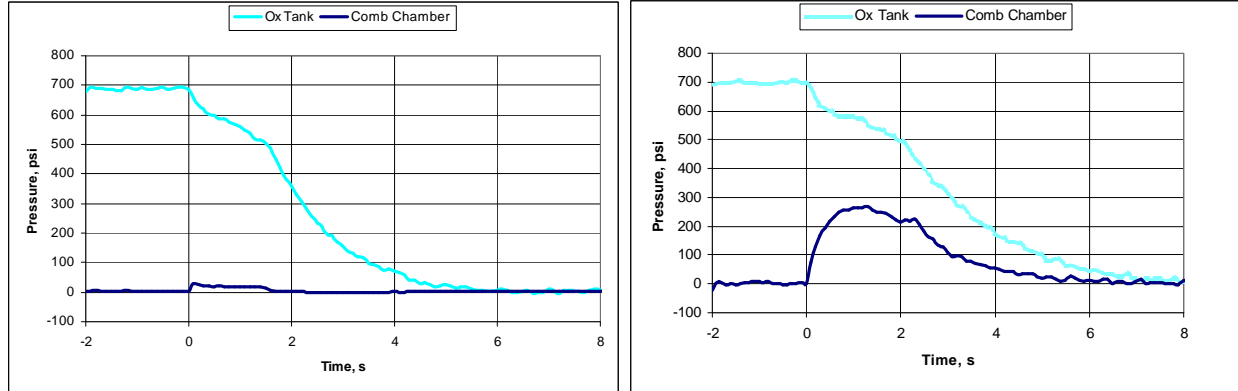

Figure 11.   Oxidizer flow testing with flight nozzle (left) and reduced-area nozzle (right).

B. Static Motor Testing

The static motor tests were performed to verify ignition system performance and gain improved estimates of regression rate and thrust. The initial tests showed a large pressure spike in the combustion chamber at the start of the burn resulting from a small detonation of the pre-melted fuel. The ignition delay (time between ignition and oxidizer valve opening) and igniter mass were reduced from 1.5 s and 8 g to 0.7 s and 4.6 g, respectively. The modifications resulted in a much less severe ignition transient (see Fig. 12).
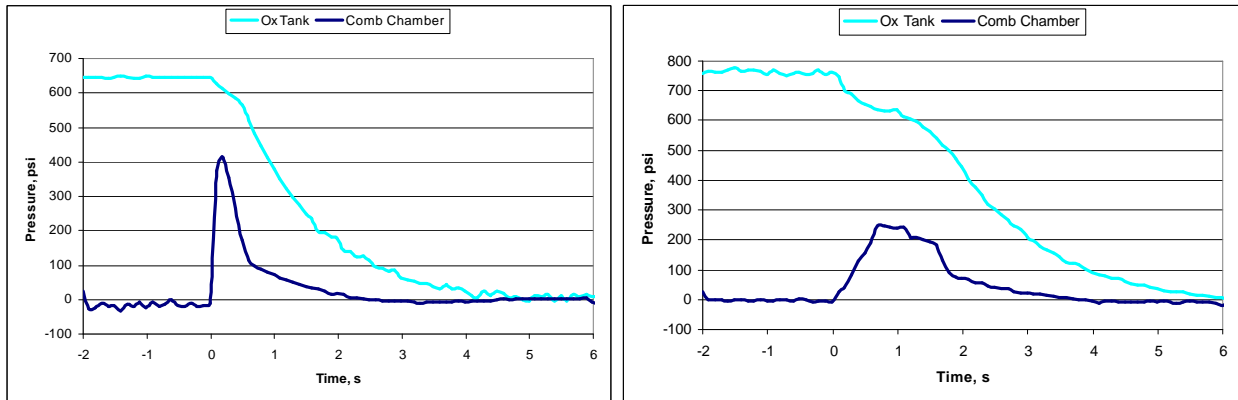

Figure 12.   Static motor testing with initial (left) and final (right) ignition sequence.

The accurate determination of the regression rate for 40% aluminized paraffin proved elusive. The regression rate appeared to be much faster than predicted based on the minimal amount of unburned fuel remaining in the combustion chamber. However, the ignition detonations on the first two static tests raised concerns about grain disintegration that could not be quantified. There was also a significant, but indeterminate amount of gaseous oxidizer burning following the liquid oxidizer phase. Furthermore, unburned fuel was witnessed dripping out of the hot combustion chamber after the tests were complete. Summing these factors together made an improved prediction of regression rate infeasible.

A load cell was used to obtain thrust data, but biasing errors were determined to be present in the set-up and the results were also deemed to be unreliable. The thrust profile was therefore estimated from the acceleration data recorded during the flight test.

V. Flight Test and Post-Flight Analysis

Flight testing was conducted at a test range in the Mojave Desert, where ground level is roughly 1,190 m above sea-level. Based on pressure data, the G-Wiz reported an apogee altitude of 2,871 m AGL. The accelerometer data, along with velocity and vertical displacement obtained by integrating that acceleration, are presented in Fig. 13. The integrated accelerometer data suggest an apogee of only 2,723 m.

The flight was recorded by two ground-based, stationary video cameras and the aft-looking onboard camera. Video confirmed that the launch system functioned properly. Onboard video was interrupted at apogee. It was assumed that the recovery ejection charge caused the camera to turn off. The rocket landed under drogue parachute only, and sustained minor damage to the ball valve faring and phenolic payload section. A commercially procured beacon, powered by one 9 V battery, was attached to the parachute bridle of the rocket. Although the rocket landed approximately 1 mile downrange, the beacon made it easy to locate.
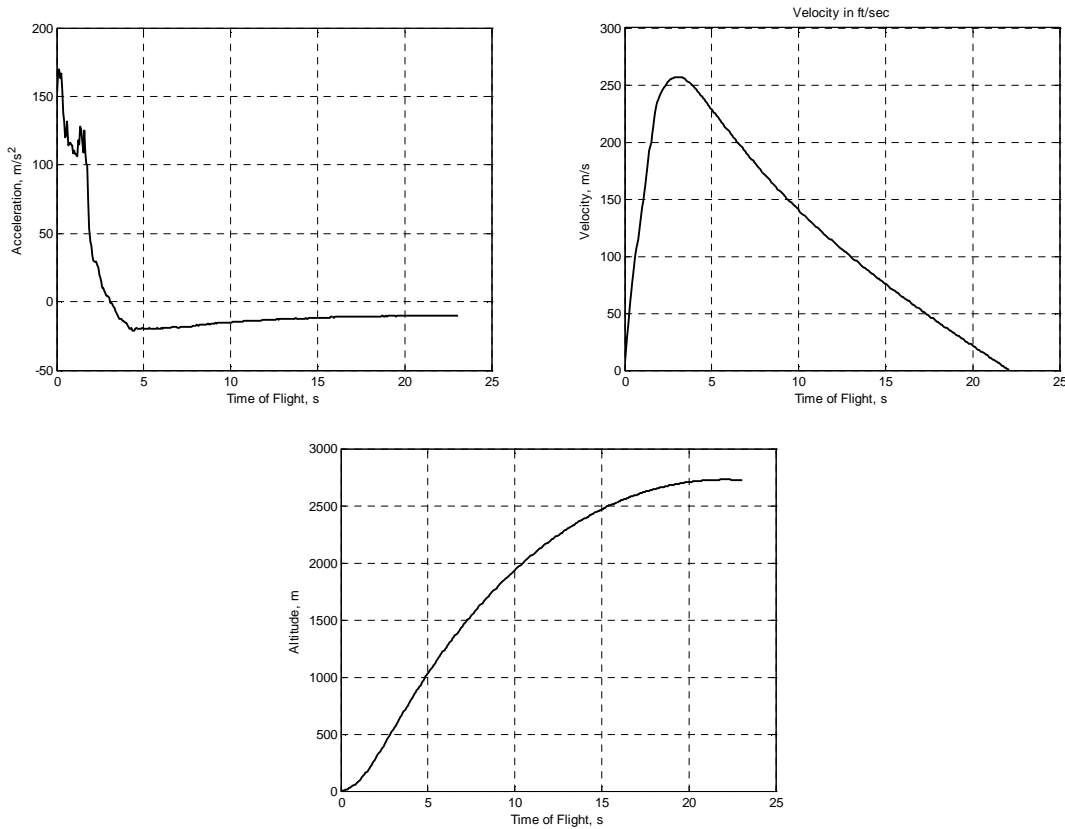

Figure 13. Flight data from launch to apogee.

The total impulse of the rocket motor was estimated from recorded acceleration flight test data. The acceleration was integrated to determine the velocity. Equations (13) and (14) used the acceleration and velocity to calculate the thrust.

$$T = m\ddot{h} + D + mg_0 \tag{13}$$

$$D = \frac{1}{2}\beta C_D S_{ref} q\dot{h}^2 \tag{14}$$

The drag coefficient C_D is dependent on Mach number (as shown in Fig. 2), which was calculated from the recorded flight data and a standard atmosphere assumption. A drag multiplier β was chosen to adjust the output of the drag model to enforce a zero thrust constraint at the end of powered flight. The coefficient β was roughly equal to 2. Since the mass expulsion rate was not precisely known, the calculation was performed twice, to give bounding values for the thrust. First, thrust was calculated with the mass constant at the preflight mass of 10.8 kg, and second with the post-flight mass of 8.0 kg. The total impulse is the time integral of the thrust curve. The calculated thrust-time curve is shown in Fig. 14 for both cases.
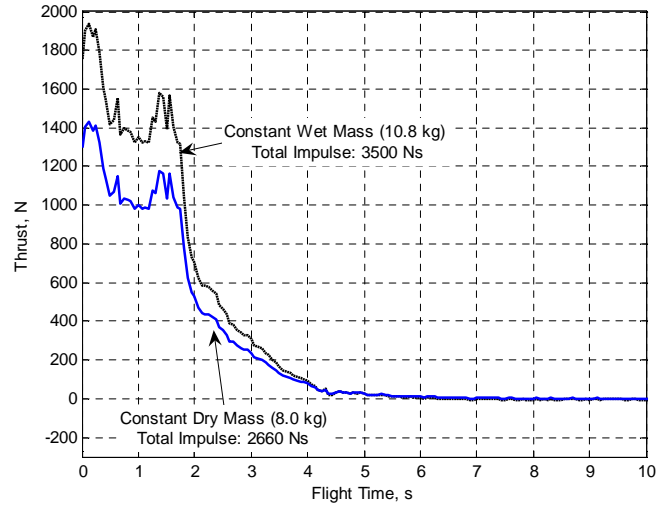

Figure 14.   Thrust and total impulse estimates from flight data.

VI. Programmatics

The entire project was completed in 8 months, starting in March and finishing in November of 2004. The original schedule called for an October launch date, but the ground test program was extended two weeks to better characterize the motor performance. This extension had a ripple effect delaying the launch approximately one month.

The total project was budgeted for $5,000, but through reuse, intelligent design, and diligent conservation effort, the entire project came to $4,300. The major cost items were: contracted machining, launch support, and electronics. The contracted machining was for tight tolerance parts and welding that was critical to the program. The launch support included a truck rental to haul and the equipment, all personal travel to and from the launch site, lodging at Mojave, and all meals.

VII.   Conclusions

Significant improvements were made over past small hybrid rocket designs, in particular the intricate simulation and modeling efforts and innovative mechanical design. The simulations were both validated and calibrated by the flight data. Novel actuation and launch systems were also successfully demonstrated. The remaining uncertainty in aluminized paraffin regression rates leaves room for much future work using this promising, high performance fuel.

Photos and videos of testing and launch, and a detailed report on the construction of the rocket subsystems are available at http://www.stanford.edu/~lichtman/Hybrids.

Appendix
Table 2.   Mass budget.

System	Item Description	Mass, kg
Recovery	86" Diameter Main Parachute & Rigging	0.34
	Rip-stop Nylon Parachute Bag	0.09
	48" Drogue parachute	0.04
	Quik links (4) and steel ring	0.102
	2 9V batteries for G-Wiz (includes electrical tape)	0.094
	20' Kevlar bridle	0.054

System	Item Description	Mass, kg
	15' Kevlar bridle	0.044
	Electric match	0.014
	Rockethunter™ Beacon	0.05
	CO_2 Cartridge and Pyro Mechanism	0.502
	Bulkhead & Tether Cutter	0.35
	Total Recovery	1.68
Airframe	Nose Cone (including aluminum tube adapter)	0.33
	Combustion Chamber with Fin Can	1.475
	36" Phenolic Tube	0.318
	Oxidizer Tank (painted; includes tube stubs, swage, and teflon tape)	2.112
	Midsection Fairing	0.244
	Total Airframe	4.479
Motor	Graphite Nozzle	0.328
	Injector Plate	0.062
	Retainer Plate (including o-ring)	0.028
	Injector Head (including tube stub, swage, and teflon tape)	0.12
	Combustion Chamber Liner (includes pre-combustion chamber and polycarbonate sleeve)	0.05
	Ball Valve	0.302
	Relief Valve	0.236
	Total Motor	1.126
Fasteners	27 #5 Button-head Screws	0.018
	6 #5 Socket-head Screws	0.006
	21 Steel Washers	0.003
	Total Fasteners	0.027
Avionics	Flight Computer (includes GPS, RF modem, and antennas)	0.1
	Flight Camera	0.1
	Flight Camera Batteries (2-AA)	0.067
	Flight Computer Battery	0.2
	Avionics Mount (includes U-bolt and 4 nuts)	0.152
	G-Wiz	0.046
	Total Avionics	0.665
Consumed Mass	Oxidizer (calculated based on 72% fill)	1.66
	Used igniters, fuel, and polycarbonate liner	1.155
	Total Consumed Mass	2.815
	Total Dry	8
	Total Wet	10.8

Acknowledgments

References

[1] Karabeyoglu, M.A., Zilliac, G., Castellucci, P., Urbanczyk, P., Stevens, J., Inalhan, G., and Cantwell, B.J. "Development of High-Burning-Rate Hybrid-Rocket-Fuel Flight Demonstrators" 39th AIAA/ASME/SAE/ASEE Joint Propulsion Conference, Huntsville, AL, July 2003.

[2] Sutton, G., Biblarz, O. *Rocket Propulsion Elements, 7th Edition*, John-Wiley & Sons, New York, 2001.

[3] Gordon, S., McBride, B. "Computer Program for Calculation of Complex Chemical Equilibrium Compositions and Applications" NASA Lewis Research Center, Cleveland, OH, October 1994.

[4] USAF Automated Missile DATCOM, Aerodynamic Methods for Missile Configurations, Software Package, Rev. 9/02, Air Force Research Laboratories, 2002.

[5] Aerolab: Rocket Drag and Stability Calculator, Version 1.3.2, Hans Olaf Toft, Denmark, 2003.

[6] Van Pelt, D., Hopkins, J., Skinner, M., Buchanan, A., Gulman, R., Chan, H., Karabeyoglu, M.A., Cantwell, B.J. "Overview of a 4-Inch OD Paraffin-Based Hybrid Sounding Rocket Program" 40th AIAA/ASME/SAE/ASEE Joint Propulsion Conference, Fort Lauderdale, FL, July 2004.